

~~Climatology, seasonality, and trends~~ A near-global climatology of oceanic coherent eddies

Josué Martínez-Moreno¹, Andrew McC. Hogg¹, and Matthew H. England²

¹Research School of Earth Science and ARC Center of Excellence for Climate Extremes, Australian National University, Canberra, Australia

²Climate Change Research Centre (CCRC), UNSW Australia, Sydney NSW, Australia

Key Points:

- Kinetic energy of coherent Coherent eddies contain around 50% of the surface ocean kinetic energy budget.
- Seasonal cycle of the number of coherent eddies and coherent eddy amplitude reveal a 3-6 month lag to wind forcing.
- Inverse cascade sets up the seasonal lag of The seasonal lag between the number and the amplitude of coherent eddies suggests a role for the inverse cascade.

14 **Abstract**

15 Ocean eddies influence regional and global climate through mixing and transport
 16 of heat and properties. One of the most recognizable and ubiquitous feature of oceanic
 17 eddies are coherent vortices with spatial scales of tens to hundreds of kilometers, frequently
 18 referred as “mesoscale eddies” ~~or “coherent eddies”~~. Coherent ~~Coherent mesoscale~~ ed-
 19 dies are known to transport properties across the ocean and to locally affect near-surface
 20 wind, cloud properties and rainfall patterns. Although coherent eddies are ubiquitous,
 21 ~~yet~~ their climatology, seasonality and long-term temporal evolution remains poorly un-
 22 derstood. ~~Thus~~Here, we examine the kinetic energy contained by coherent eddies and
 23 ~~we present the annual~~ present the seasonal, inter-annual and long-term ~~changes of automatically~~
 24 ~~identified coherent eddies variability of ~37 million coherent eddies features detected~~ from
 25 satellite observations ~~from~~ between 1993 to 2019. Around 50% of the kinetic energy con-
 26 tained by ocean eddies corresponds to coherent eddies. Additionally, a strong ~~hemispherical~~
 27 seasonal cycle is observed, with a 3–6 months lag between the wind forcing and the re-
 28 sponse of the coherent eddy field. ~~Furthermore,~~ the ~~The~~ seasonality of the number of co-
 29 herent eddies and their amplitude reveals that the number of coherent eddies responds
 30 faster to the forcing (~3 months), than the coherent eddy amplitude (which is lagged
 31 by ~6 months). This seasonal cycle of the coherent eddy properties is spatially variable,
 32 thus we also analyse the coherent eddy climatology in key oceanic regions. Our analy-
 33 sis highlights the relative importance of the coherent eddy field in the ocean kinetic en-
 34 ergy budget, implies a strong response of the eddy number and eddy amplitude to forc-
 35 ing at different time-scales, and showcases the seasonality, and multidecadal trends of
 36 coherent eddy properties.

37 **Plain language summary**

38 Coherent eddies are the most common feature ~~in the oceans of ocean variability~~
 39 observable from satellites. They are crucial in ocean dynamics as they can transport prop-
 40 erties over long distances and interact with the atmosphere. Our study investigates the
 41 seasonal, interannual, and long-term changes in the abundance and intensity of coher-
 42 ent eddies, by automatically identifying individual eddies over the available satellite al-
 43 timeter record. The seasonal cycle suggests a transition from numerous, smaller, and weaker
 44 coherent eddies, to fewer and larger, and stronger coherent eddies over the season. In

45 addition, a long-term adjustment of the coherent eddy field is identified ~~possible due with~~
 46 possible links to long-term changes in the climate system.

47 1 Introduction

48 Mesoscale ocean variability with spatial scales of tens to hundreds of kilometers is
 49 comprised of processes such as vortices, waves, and jets (Ferrari & Wunsch, 2009; Fu et
 50 al., 2010). These mesoscale processes are highly energetic, and they play a crucial role
 51 in the transport of heat, salt, momentum, and other tracers through the ocean (Wun-
 52 sch & Ferrari, 2004; Wyrtki et al., 1976; Gill et al., 1974). ~~Possibly, One of~~ the most rec-
 53ognizable and abundant ~~process observed from satellites is ocean processes observable~~
 54 from space are mesoscale vortices. Although mesoscale vortices are commonly referred
 55 to in the literature as “mesoscale eddies”, this term is also often used to describe the to-
 56 tal mesoscale ocean variability (the time-varying component of the mesoscale flow), thus,
 57 ~~here to avoid ambiguity~~ we will refer to mesoscale vortices as *coherent eddies*. Coherent
 58 eddies are abundant and energetic; therefore they are also essential to ocean dynamics
 59 as concluded by many previous studies (Hogg & Blundell, 2006; Siegel et al., 2011; Beron-Vera et al., 2013; Frenge
 60 z

61 Coherent eddies are quasi-circular geostrophic currents. According to their rota-
 62 tional direction and the sign of the Coriolis parameter, the sea surface height anomaly
 63 within a coherent eddy can have a negative or positive sea surface height anomaly (cold-
 64 core and warm-core coherent eddies, respectively). This characteristic sea surface height
 65 signature of coherent eddies has been utilized to ~~automatically~~ identify and track coher-
 66 ent eddies from satellite altimetry (~~Cui et al., 2020; Martínez-Moreno et al., 2019; Ashkezari et al., 2016; Faghmou~~
 67 ~~.(e.g., Chelton et al., 2007; Faghmous et al., 2015; Ashkezari et al., 2016; Martínez-Moreno et al., 2019; Cui et al.,~~
 68). Automated identification algorithms of coherent eddies have shown revealed their ubiq-
 69 uity in the oceans, with a predominant influence at hotspots of eddy activity such as boundary
 70 in boundary current extensions and the Antarctic Circumpolar Current. In these regions,
 71 ~~Chelton et al. (2011) it has been~~ estimated that coherent eddies contribute around 40–
 72 50% of the net mesoscale kinetic energy (Chelton et al., 2011) and thus a significant frac-
 73 tion of the total kinetic energy (Ferrari & Wunsch, 2009). Although this ~~unique~~ estimate
 74 showcases the importance of the mesoscale coherent eddy field, the energy contained by
 75 coherent eddies was estimated by extracting the ~~geostrophic velocities within the detected~~
 76 ~~coherent eddies, thus total geostrophic velocity within the radius of each detected coherent~~

77 eddy; thus, it is possible ~~it that this estimate~~ may contain energy from other processes.
 78 ~~Coherent eddies are not only abundant and may have a large proportion of the surface~~
 79 ~~kinetic energy budget, but they are also essential to ocean dynamics as concluded by many~~
 80 ~~previous studies (Patel et al., 2020; Schubert et al., 2019; Pilo et al., 2015; Frenger et al., 2015, 2013; Beron-Vera et al., 2013).~~
 81 Here we extend on this past work by reconstructing the surface imprint of coherent eddies
 82 using a new eddy tracking algorithm and using the latest available satellite record.

83 There is broad consensus that mesoscale eddy kinetic energy has a pronounced sea-
 84 sonal variability (~~Uehida et al., 2017; Kang & Curchitser, 2017; Qiu & Chen, 2004; Qiu, 1999~~)
 85 (~~Qiu, 1999; Qiu & Chen, 2004; Kang & Curchitser, 2017; Uehida et al., 2017~~). Several
 86 hypotheses have been proposed to explain this seasonality including: seasonal variations
 87 of atmospheric forcing (Sasaki et al., 2014), seasonality of the mixed layer depth (Qiu
 88 et al., 2014; Callies et al., 2015), seasonality of the intensity of barotropic instability (Qiu
 89 & Chen, 2004), the variability of the baroclinic instability due to the seasonality of the
 90 vertical shear (Qiu, 1999), and a seasonal lag of the inverse energy cascade (i.e. energy
 91 is transported between scales, from small to large; Arbic et al., 2013) in combination with
 92 the presence of a front in the mixed layer, which can lead to a seasonal cycle of the baro-
 93 clinic instability (Qiu et al., 2014). On one hand, processes such as barotropic and baro-
 94 clinic instabilities control the seasonality of coherent eddies in the ocean. On the other
 95 hand, recent studies using observations and eddy-permitting climate models suggest sev-
 96 eral long-term adjustments of the global ocean capable of long-term changes in the co-
 97 herent eddy field. Such readjustments include a multidecadal increase in the ocean strat-
 98 ification ~~resulted resulting~~ from temperature and salinity changes (Li et al., 2020), a hor-
 99 izontal readjustment of ~~the~~ sea surface temperature gradients (~~Ruela et al., 2020; Bouali et al., 2017; Cane et al., 1997~~;
 100 ~~(Cane et al., 1997; Bouali et al., 2017; Ruela et al., 2020)~~, and an intensification of the
 101 kinetic energy, eddy kinetic energy, and mesoscale eddy kinetic energy over the last 3 decades
 102 as a consequence of an increase in wind forcing (Hu et al., 2020; Wunsch, 2020; Martínez-
 103 Moreno et al., 2021). All these seasonal factors and long-term readjustments directly in-
 104 fluence the annual and decadal response of the coherent eddy field, however, the season-
 105 ality of the coherent component of the eddy kinetic energy, as well as the seasonal cy-
 106 cle and trends of the coherent eddy statistics, remain unknown.

107 Here we present a new global climatology of the coherent eddy kinetic energy by
 108 reconstructing the coherent eddy signature from satellite observations. Our study doc-
 109 documents the seasonal cycle of the coherent eddy kinetic energy, and the seasonal cycle and

long-term trends of the coherent eddy properties over the satellite record. Moreover, we conduct more ~~detail analysis~~detailed analyses in regions where coherent eddies dominate the eddy kinetic energy field. ~~This~~The rest of this paper is structured as follows: the data sources and methodology are described in ~~section~~Section 2. Then, we present the climatology, energy ratios, and global seasonality of the coherent eddy kinetic energy in ~~section~~Section 3. Section 4 ~~presents outlines~~ the global climatology and seasonality of coherent eddy properties, followed by long-term changes of the coherent eddy properties (~~section~~Section 5). Then we focus our attention on the seasonal cycle and coherent eddy properties in regions dominated by coherent eddies (~~section~~Section 6). Finally, ~~section~~Section 7 summarizes the main results and discusses the implications of this study.

2 Methods

We use daily sea surface height (SSH) data made available by the Copernicus Marine Environment Monitoring Service in near real time (CMEMS, 2017). This gridded product contains the sea surface height and geostrophic velocities with daily 0.25° resolution from January 1993 to 2019. The daily geostrophic velocities ~~allowed~~allow us to compute the kinetic energy (KE) and eddy kinetic energy (EKE) over the satellite record. The main source of EKE is the time-varying wind (Ferrari & Wunsch, 2009), ~~thus we computed~~; thus, we also compute the seasonal cycle of the wind magnitude from the JRA55 reanalysis (Japan Meteorological Agency, Japan, 2013) using wind velocities at 10m above the ocean's surface.

Over the same record, coherent eddy statistics from Martínez-Moreno et al. (2019), hereafter ~~M-MM~~MM19, are analyzed and compared ~~to with~~ those released by Chelton & Schlax (2013), ~~both~~hereafter CS13. ~~Both~~ datasets are gridded in a 1° resolution ~~Although both datasets and~~ are produced via automated eddy identification algorithms using closed contours of SSH. ~~However~~, these datasets have important differences in the criteria they use to identify and record coherent eddy statistics. The major differences include: (i) ~~M-MM~~MM19's algorithm requires an adjustment between a 2D Gaussian and the SSH anomaly (SSHa) surface within the ~~identify identified~~ closed contour, while ~~Chelton~~CS13's only uses the ~~outer-most outermost~~ closed contour of SSH; (ii) ~~M-MM~~MM19's dataset reports the maximum SSHa within the identified coherent eddy, while ~~Chelton~~CS13's algorithm reports the maximum SSH value minus the discrete level in which the coherent eddy was identified; ~~M-M and~~ (iii) MM19's dataset includes all detected coherent eddies, while ~~Chelton~~CS13's

dataset excludes (iii) coherent eddies with lifetimes shorter than four weeks and (iv) coherent eddy amplitudes smaller than 1cm. Moreover, M-M MM19's algorithm allows the reconstruction of the coherent eddy field under the assumption that coherent eddies have a 2D Gaussian imprint in the sea surface height. This Gaussian reconstruction of the coherent eddy field then ~~allow~~ allows us to estimate the coherent geostrophic eddy velocities and thus the kinetic energy contained only by coherent eddies.

2.1 Kinetic Energy decomposition

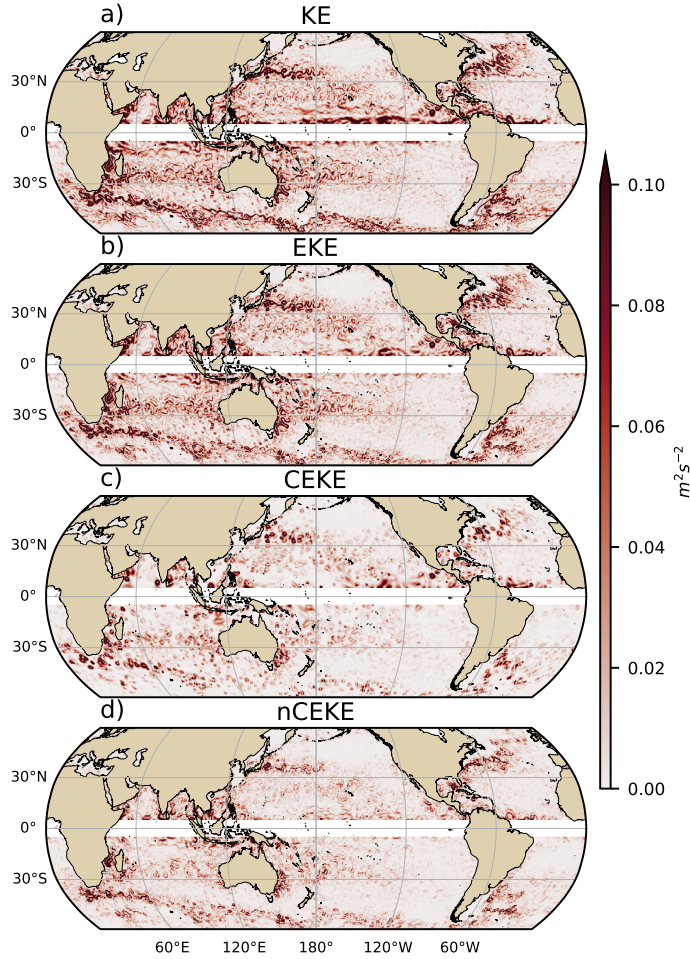
Kinetic energy is commonly divided into the mean and time-varying components through a Reynolds decomposition. At a given time, the surface velocity field $\mathbf{u} = (u, v)$ is split into the time mean ($\bar{\mathbf{u}}$) and time varying components (\mathbf{u}'). Moreover, M-M MM19 proposed to further decompose the eddy kinetic energy into the energy contained by coherent features (\mathbf{u}'_e) and non-coherent features (\mathbf{u}'_n). Therefore the KE equation can be written as:

$$\text{KE} = \underbrace{\bar{u}^2 + \bar{v}^2}_{\text{MKE}} + \underbrace{u'_e^2 + v'_e^2}_{\text{CEKE}} + \underbrace{u'_n^2 + v'_n^2}_{\text{nCEKE}} + \mathcal{O}_c^2 + \mathcal{O}^2 \quad (1)$$

Due to the properties of this decomposition, the second order term \mathcal{O}^2 is zero when averaged over the same period as $\bar{\mathbf{u}}$. However, \mathcal{O}_c^2 is not ~~necessarily~~ necessarily negligible, unless it is averaged over time and space. More information about the decomposition of the field into coherent features and non-coherent features is explained ~~by~~ in Martínez- Moreno et al. (2019). A global snapshot of each component of kinetic energy decomposition is shown in Figure 1, where the KE and EKE are comprised of rings and filaments. As expected, the decomposition of EKE into CEKE and nCEKE components ~~exhibit~~ exhibits only ring-like signatures expected of coherent eddies, while the non-coherent component shows ~~filaments and some miss-identified~~ primarily ~~filaments, with some mis-identified~~ coherent eddies.

2.2 Eddy statistics

The eddy statistics used in this study include (i) the eddy count ($cEddy_n$) defined as the number of coherent eddies per grid cell, (ii) the eddy diameter defined as the di-



165 **Figure 1.** Snapshot of surface kinetic energy (\bar{KE}), surface eddy kinetic energy (\bar{EKE}),
 166 surface coherent eddy kinetic energy (\bar{CEKE}), and surface non-coherent eddy kinetic energy
 167 (\bar{nCEKE}) for the 1st of January 2017.

171 ameter of a circle with equal area as to the closed contour of each identified eddy, and
 172 (iii) the mean eddy amplitude defined as the mean amplitude of the coherent eddies within
 173 the cell ($cEddy_{amp}$). The latter metric can be separated into positive ($cEddy_{amp}^+$) and
 174 negative ($cEddy_{amp}^-$) coherent eddy amplitudes, defined as the mean amplitude of warm
 175 core and cold core coherent eddies, respectively, within the cell. The polarity indepen-
 176 dent eddy amplitude ($|cEddy_{amp}|$) is defined as:

$$|cEddy_{amp}| = \frac{1}{2} (cEddy_{amp}^+ - cEddy_{amp}^-) \quad (2)$$

177 Note that the $cEddy_{amp}^+$ and $cEddy_{amp}^-$ are sign definite, thus the difference will always
 178 be positive, whereas the gridded averaged $cEddy_{amp}$ can be negative or positive noting

179 the dominant polarity of coherent eddies in the region, and the absolute value of $cEddy_{amp}$
 180 is denoted by $cEddy_{|amp|}$. We analyze the climatology ~~, seasonal cycles~~ and trends of the
 181 ~~eddy statistics above eddy statistics over the available satellite record, namely~~ between
 182 1993 and 2019. We exclude the equatorial region ($10^{\circ}\text{S} - 10^{\circ}\text{N}$) and regions poleward
 183 of 60° , because the geostrophic approximation is invalid near the equator and the satellite
 184 spatial coverage at high-latitudes is unable to resolve the coherent eddy scales polewards
 185 of 60° . Note that the climatology of $cEddy_n$ is computed by adding all the identified ed-
 186 dries over the record, while all other climatological statistics are computed as the time-
 187 average over the record. Seasonal climatologies are calculated for the monthly average
 188 of each coherent eddy statistic, while hemispherical time-series are filtered with a run-
 189 ning average of 90 days. Trends of $cEddy_n$ and $|cEddy_{amp}|$ are calculated by coarsen-
 190 ing the dataset to a 5° grid, and then linear trends are computed for each grid point, ~~the~~
 191 ~~statistical significance~~. The statistical significance of trends is assessed by a modified
 192 Mann-Kendall test above 95% confidence level (Yue & Wang, 2004).

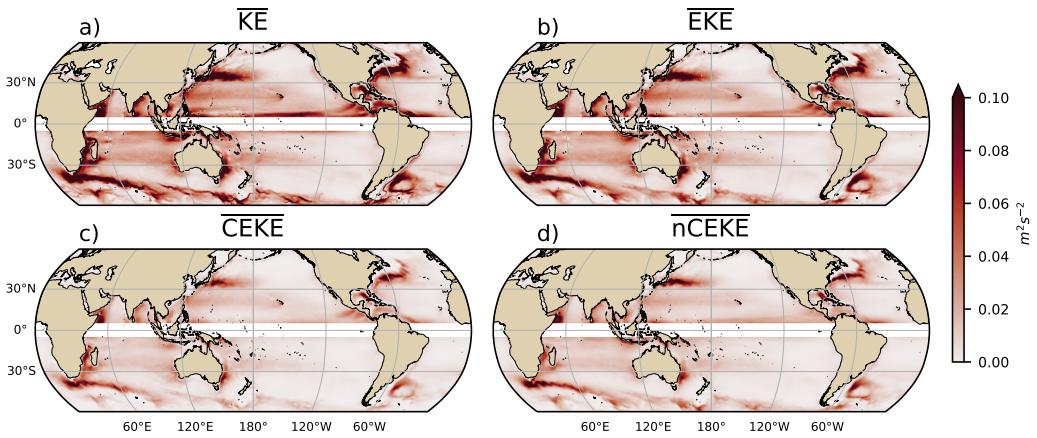
193 Time averages are denoted by $\overline{}$, while area-weighted averages are denoted using
 194 $\langle \rangle$, ~~the area weighted of~~ where the area-weighted average of a function f is:

$$\langle f \rangle = \frac{\int f dx dy}{\int dx dy} \frac{\int f \xi dx dy}{\int \xi dx dy}, \quad (3)$$

195 ~~area-weighted coherent eddy properties masked areas each time, where ξ is a mask~~
 196 ~~that is set to zero in grid cells where~~ no coherent eddies were identified.

197 3 Global Coherent Eddy Energetics

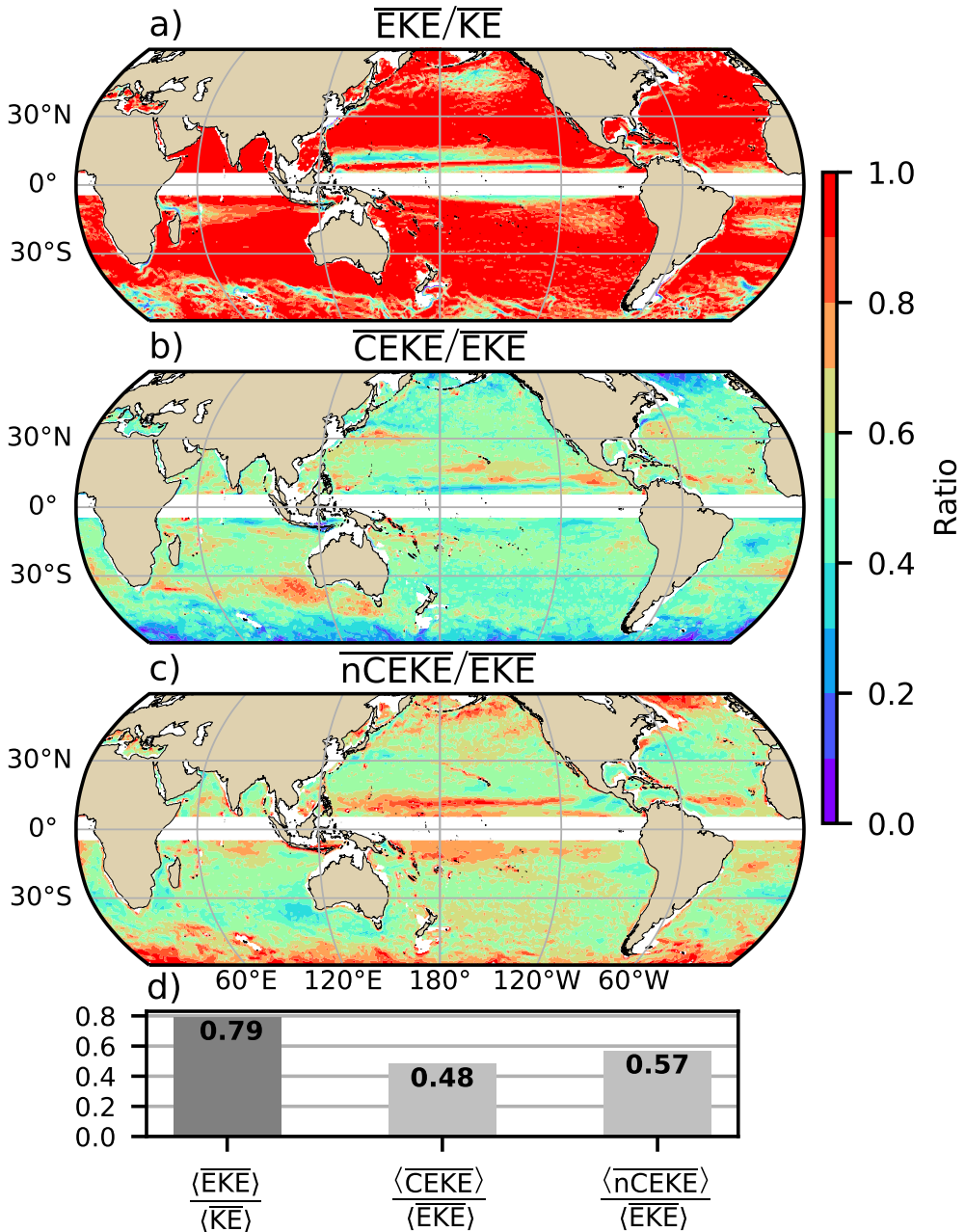
198 The kinetic energy decomposition estimated from sea surface height measured by
 199 satellite altimeters averaged from 1993-2019 is shown in Figure 2. These maps show that
 200 many regions of the global ocean are highly energetic in mean KE (\bar{KE}), mean EKE (\bar{EKE}),
 201 mean coherent eddy kinetic energy (\bar{CEKE}) and mean non-coherent eddy kinetic energy
 202 (\bar{nCEKE}). The spatial pattern highlights ~~well known~~ well-known regions of the ocean
 203 where mesoscale processes are abundant, such as the western boundary ~~extensions current~~
 204 extensions (WBCe) and the Antarctic Circumpolar Current. ~~Remarkably, the~~ The spa-
 205 tial distribution of the energy contained by the reconstructed mesoscale coherent eddies
 206 and non-coherent components are similar (Figures 2c,d). However, there are some re-
 207 gions where coherent eddies dominate over non-coherent, and vice-versa. Overall, this
 208 decomposition ~~suggest~~ suggests that boundary current extensions and other energetic



211 **Figure 2.** Mean surface kinetic energy (\overline{KE}), surface eddy kinetic energy (\overline{EKE}), surface
 212 coherent eddy kinetic energy (\overline{CEKE}), and surface non-coherent eddy kinetic energy (\overline{nCEKE})
 213 averaged between 1993-2018.

209 regions, in particularly, of the ocean, particularly eddy-rich regionsin the ocean, contain
 210 both coherent and non-coherent components of the kinetic energy.

223 Eddy kinetic energy is known to be more than an order of magnitude greater than
 224 kinetic energy of the mean flow (MKE(Gill et al., 1974); Gill et al. 1974); this result
 225 is clearly shown in Figure 3a, where which indicates that \overline{EKE} is responsible for almost
 226 all the \overline{KE} across the ocean, except for regions with persistent currents over time. Such
 227 regions are located in the mean boundary extension locations, the equatorial Pacific cur-
 228 rents and regions in the Antarctic Circumpolar Current, where the \overline{EKE} explains around
 229 40% of the \overline{KE} . In a previous study, Chelton et al. (2011) estimated that the EKE within
 230 coherent eddies with lifetimes greater than 4 weeks contain between 40 to 60 percent 40-60%
 231 of the \overline{EKE} . Our method to reconstruct the coherent eddy signature (Figure 3b) further
 232 corroborates that the coherent eddy component ($\langle \overline{CEKE} \rangle$) has ~48% of the $\langle \overline{KE} \rangle$ (Fig-
 233 ure 3d). Furthermore, global area averages of the ratios show that $\langle \overline{EKE} \rangle$ explains ~78%
 234 of the ocean $\langle \overline{KE} \rangle$ field, while non coherent eddy features contain ~57% percent of the
 235 $\langle \overline{EKE} \rangle$. Note that the globally averaged coherent and non coherent components do not
 236 add to 100% as the cross terms (\mathcal{O}_c^2) are non-zero, due to and coherent eddy reconstruc-
 237 tion errors. The spatial pattern reveals a dominance of the \overline{CEKE} equatorward from the
 238 boundary extensions and current extensions and in areas with large coherent eddy con-
 239 tributions of around 80% of the region's eddy kinetic energycan be found, such as south



214 **Figure 3.** Ratios of the kinetic energy components. a) Map of the proportion of mean eddy
 215 kinetic energy (\overline{EKE}) versus mean kinetic energy (\overline{KE}); b) Map of the percentage of mean co-
 216 herent eddy kinetic energy (\overline{CEKE}) versus mean eddy kinetic energy (\overline{EKE}); c) Map of the
 217 percentage of mean non-coherent eddy kinetic energy (\overline{nCEKE}) versus mean eddy kinetic energy
 218 (\overline{EKE}); d) Global time and area averaged (represented by $\langle \rangle$) percentage of mean eddy kinetic
 219 energy ($\langle \overline{EKE} \rangle$) versus the global mean kinetic energy ($\langle \overline{KE} \rangle$), area averaged percentage of mean
 220 coherent eddy kinetic energy ($\langle \overline{CEKE} \rangle$) and mean non coherent eddy kinetic energy ($\langle \overline{nCEKE} \rangle$)
 221 versus global mean eddy kinetic energy ($\langle \overline{EKE} \rangle$). Regions where the depth of the ocean is shall-
 222 lower than 1000m are removed from the ratio estimation.

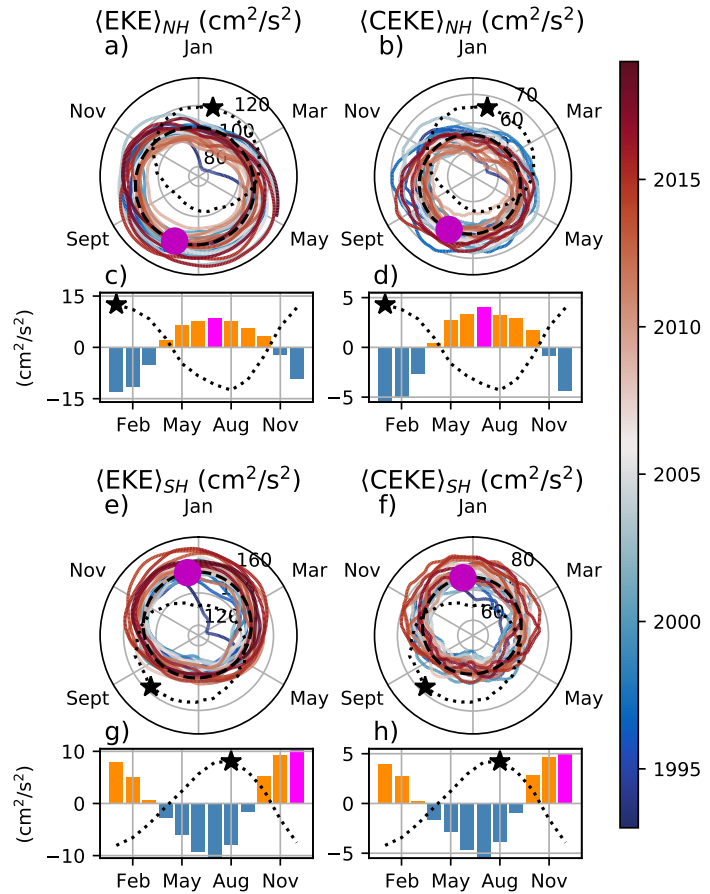
of Australia, in the Tehuantepec Gulf, and in the tropical Atlantic. An evident signal is an-a reduction of the energy contained by coherent eddies at high latitudes and an increase in the energy explained by non-coherent eddies; this signal could be a consequence of the incapability-inability of the 0.25° satellite resolution (~ 13 km at 60° latitude) to resolve coherent eddies with scales smaller than ~ 10 km (first baroclinic Rossby radius at 60° ; Chelton et al. 1998).

Figure 4 shows the seasonal cycle of the area weighted EKE and CEKE for the Northern Hemisphere ($\langle \text{EKE} \rangle_{NH}$ and $\langle \text{CEKE} \rangle_{NH}$; $10^{\circ}\text{N} - 60^{\circ}\text{N}$) and Southern Hemisphere ($\langle \text{EKE} \rangle_{SH}$ and $\langle \text{CEKE} \rangle_{SH}$; $60^{\circ}\text{S} - 10^{\circ}\text{S}$). In both hemispheres, the $\langle \text{EKE} \rangle$ and $\langle \text{CEKE} \rangle$ peak during summer. In the Northern Hemisphere, the largest $\langle \text{EKE} \rangle_{NH}$ and $\langle \text{CEKE} \rangle_{NH}$ occurs in July, ~ 6 months after the maximum winds in January (purple bar and back star in Figure 4c and d). Meanwhile, the Southern Ocean $\langle \text{EKE} \rangle_{SH}$ and $\langle \text{CEKE} \rangle_{SH}$ seasonal maxima arises during December, ~ 4 months after the maximum winds in August (purple bar and back star in Figure 4g, and h). This lag between winds and the eddy and coherent eddy energy components is further discussed in section Section 4.

The cyclic plots in Figure 4 show the temporal evolution of $\langle \text{EKE} \rangle$ and $\langle \text{CEKE} \rangle$. Note that high frequency variability can be observed in the $\langle \text{CEKE} \rangle$ field with temporal scales of a few months, this variability could be attributed local-to regional dynamics averaged over the hemisphere -(boundary currents, ocean gyres, etc.), as well as errors within the coherent eddy reconstruction. Additionally, concentric changes in the cyclic plots highlight long-term changes over the record. For example, the Northern Hemisphere winters in-during early years of the record (blue) had a more energetic coherent eddy field, which has transitioned to weaker coherent energy eontents-content since 2010 (red), in other words, the intensity of the $\langle \text{CEKE} \rangle_{NH}$ field has decreased. A larger long-term change can be observed in the Southern Hemisphere, where concentric growth over time in $\langle \text{EKE} \rangle_{SH}$ and $\langle \text{CEKE} \rangle_{SH}$ support the previously observed strengthening of the eddy field in the Southern Ocean (Hogg et al., 2015; Martínez-Moreno et al., 2019; Martínez-Moreno et al., 2021).

4 Global Coherent Eddy Statistics

Coherent eddy kinetic energy allows us to quantify and study the energy of the eddy field, but the coherent eddy properties computed by automated coherent eddy identi-



268 **Figure 4.** Seasonality of the ~~area-weighted~~^{area-weighted} ~~area-weighted~~^{area-weighted} eddy kinetic energy ($\langle EKE \rangle$) ~~and~~^{and}
 269 coherent eddy kinetic energy ($\langle CEKE \rangle$). Panels a) and b) show the time-series of the North-
 270 ern Hemisphere, while panels e) and f) correspond to the Southern Hemisphere. Panels c) and
 271 d) show the seasonal cycle of the $\langle EKE \rangle_{NH}$ and $\langle CEKE \rangle_{NH}$ in the Northern Hemisphere, and
 272 panels g) and h) show the Southern Hemisphere ($\langle EKE \rangle_{SH}$ and $\langle CEKE \rangle_{SH}$). Dashed lines cor-
 273 respond to the seasonal cycle of the fields and dotted lines show the seasonal cycle of the wind
 274 magnitude smoothed over 120 days (moving average). The black and magenta markers (circle
 275 and bar) show the maximum of the seasonal cycle for the kinetic energy components and the
 276 wind magnitude, respectively. In the cyclic plots, line colors shows the year.

fication algorithms allow us to further investigate in more detail the contribution and
 temporal changes of their abundance (i.e. the number of eddies) and their intensity (both
 their amplitude and diameter). Figure 5 shows gridded climatologies of the number of
 eddies and the eddy amplitude. We contrast our MM19 In this analysis, we contrast our
 MM19 eddy count with Chelton et al. (2007) (that of CS13 (Chelton et al., 2007; Fig-
 ure 5a-b). Although the number of the identified eddies is larger in MM19, possi-
 bly due to the lifespan filter implemented by CheltonCS13, both datasets reveal consis-
 tent spatial patterns. For example, both datasets show high an important zonal variation
 in the abundance of eddies in the with high numbers of eddies in mid-latitudes and fewer
 eddies in the tropics and at high-latitudes (~60°). Additionally, there is a tendency at
 mid-latitudes (30°) of higher number of eddies in the eastern side of ocean basins (e.g.
 East North Pacific, East North Atlantic, as well as the East South Pacific, and East South
 Atlantic and East Indian Ocean, and small number counts of eddies in the tropics and
 in high latitudes (~60°). An interesting pattern also). Another interesting pattern emerges
 in both eddy count datasets, where small scale structures with larger eddy counts are
 favored across the ocean. In addition, to preferential appear in the eddy count field. These
 small structures highlight preferred coherent eddy paths observable in boundary extensions
 and regions in current extensions and over regions of the Southern Ocean. These clusters
 structures and paths of coherent eddies could be associated with topographic features,
 however they remain a puzzling with overall consistency between the eddy count pattern
 using these two patterns using the two different eddy identification methods.

Regions with large counts of eddies have in general small absolute amplitudes (Figure 5 c). The ocean gyre interiors follow with have a larger absolute amplitude and fi-
 nally regions such as the boundary extensions and current extensions and the Antarctic
 Circumpolar Current have the largest coherent eddy absolute amplitudes as shown
 , as shown also by Chelton et al. (2011). Eddy amplitude highlights regions dominated
 by a given coherent eddy polarity, for example, boundary extensions have a preferred sign
 (Figure 5 d); namely, positive amplitude polewards of the boundary current extension
 mean location, and negative amplitude equatorwards. This sign preference is consistent
 with the preferential way that coherent eddies are shed from boundary extensions; current
 extensions; with warm core eddies (positive) polewards of the boundary current exten-
 sion, and equatorward for cold core eddies (negative) (Kang & Curchitser, 2013; Chel-
 ton et al., 2011, 2007). These global statistics reveal the absolute coherent eddy ampli-

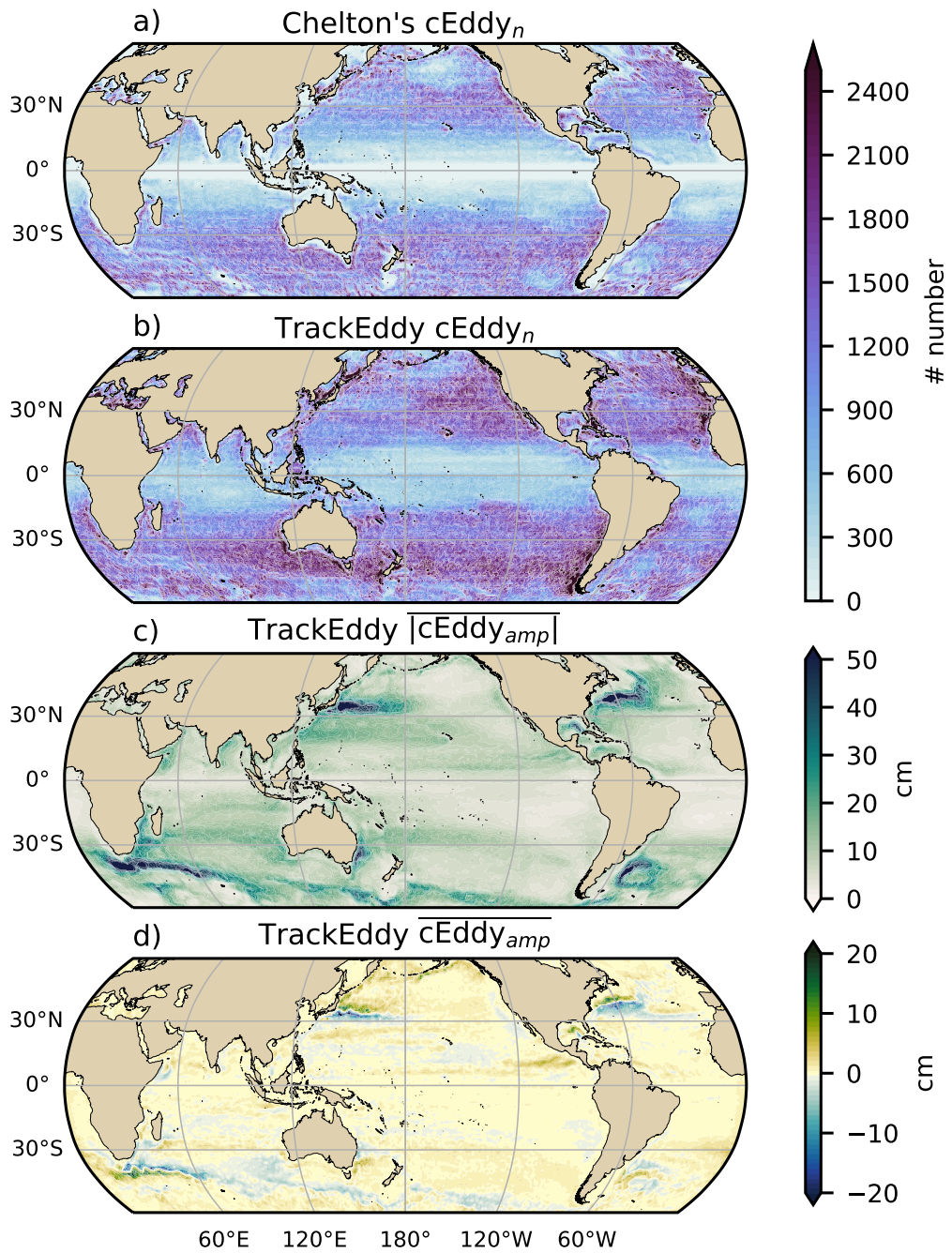


Figure 5. Averaged coherent eddy statistics. a) Climatology of the number of coherent eddies ($cEddy_n$) identified by Chelton et al. (2007); b) Climatology of the number of coherent eddies ($cEddy_n$) identified by Martínez-Moreno et al. (2019); c) Climatology of the mean absolute coherent eddy amplitude ($cEddy_{amp}$). d) Climatology of the mean coherent eddy amplitude ($cEddy_{amp}$).

318 tude ~~is-a proxy-of~~as a proxy for the CEKE with similar spatial patterns (Figure 2 & Fig-
 319 ure 5c) and showcases that regions where ~~CEKE~~ has a large proportion of ~~EKE~~ (Fig-
 320 ure 3), the absolute coherent eddy amplitude is also large.

321 To further understand the seasonal cycle of $\langle \text{CEKE} \rangle$, we compute the climatology
 322 of coherent eddy properties in each hemisphere (Figure 6). The seasonality of the num-
 323 ber of eddies in the Northern Hemisphere peaks ~~on-in~~ April (Figure 6-a, c), while the
 324 Southern Hemisphere maximum number of eddies occurs during October (Figure 6-e,
 325 g). Meanwhile, the seasonality of the ~~polarity independent~~ eddy amplitude ($\langle |c\text{Eddy}_{amp}| \rangle$)
 326 peaks in August and January for the Northern and Southern Hemispheres respectively
 327 (Figure 6-b, d, f, and h). As expected, the seasonality of $\langle |c\text{Eddy}_{amp}| \rangle$ ~~xw, or~~ equivalent
 328 to the intensity of the coherent eddies, is consistent with the seasonal cycle of $\langle \text{CEKE} \rangle$.
 329 **Furthermore,**

330 **A key feature of Figure 6 is** a distinct lag of ~ 3 months ~~is observed~~ between the
 331 winds and eddy count, while the eddy amplitude maximum occurs ~ 6 months after the
 332 seasonal maxima in winds. We ~~observe suggest that~~ the eddy number increases earlier
 333 in the year and ~~through~~ eddy-eddy interactions (merging of coherent eddies),~~the~~ the am-
 334 plitude of the coherent eddy increases ~ 3 months after. This seasonal lag and summer
 335 maxima is consistent with **Figure 5, furthermore, previous studies**previous studies which
 336 suggest that a time-lag of the inverse cascade (Sasaki et al., 2014; Qiu et al., 2014) is re-
 337 sponsible ~~of for~~ the EKE seasonal cycle, where winter has the highest energy at the small-
 338 est scales (non-resolvable with satellite observations), spring and autumn have the high-
 339 est and lowest energy ~~in at~~ scales of 50-100 km, and summertime has the highest energy
 340 at the largest scales (> 100 km; Uchida et al. 2017). Thus, the maximum of $\langle \text{EKE} \rangle$, $\langle \text{CEKE} \rangle$,
 341 and $\langle |c\text{Eddy}_{amp}| \rangle$ located during summertime ~~suggest suggests~~ that the seasonality of
 342 eddies and coherent eddies could be dominated by scales larger than 100 km.

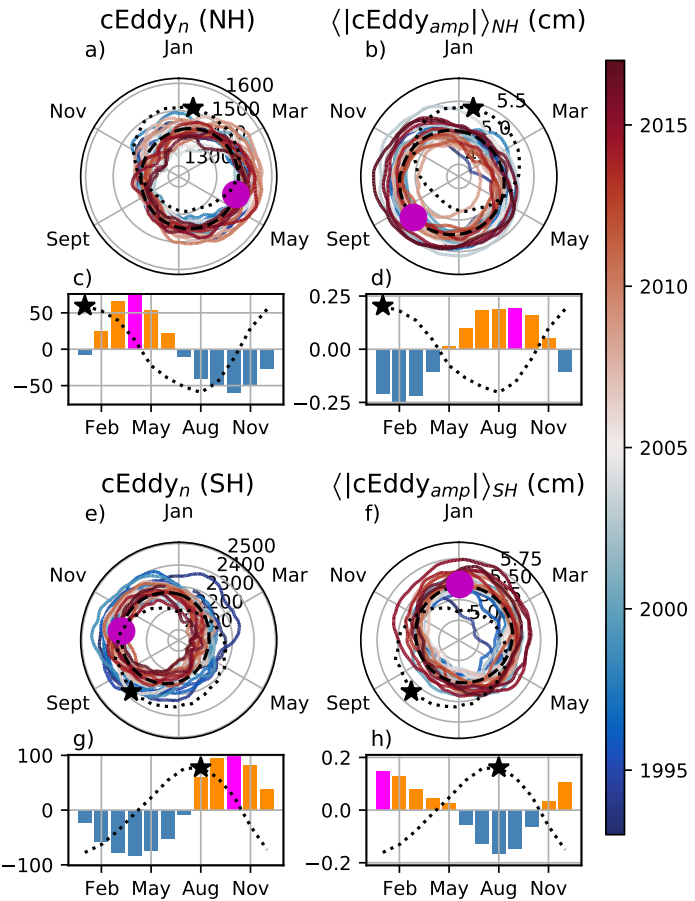
343 This result can be further explored by looking at the seasonal evolution of the eddy
 344 diameter ($c\text{Eddy}_d$). Note that 90% of identified coherent eddies have diameters between
 345 50 to 220 km (Figure 7-a). We ~~divided partition~~ eddies into large-scale coherent eddies
 346 (diameter > 120 km) and small-scale coherent eddies (diameter < 120 km; Figure 7a).
 347 In the Northern Hemisphere, ~~small small-scale~~ eddies have a seasonal peak in diameter
 348 during May, while ~~large large-scale~~ eddies have the greatest diameter in September (Fig-
 349 ure 7-b). Meanwhile, in the Southern Hemisphere, the small-scale coherent eddies ~~have~~

350 ~~the exhibit~~ maximum diameter in December, while ~~the diameter of~~ large-scale coherent
 351 eddies ~~peak peaks~~ in February (Figure 7 c). This result suggests that wind driven baro-
 352 clinic instabilities generate small coherent eddies early in the season, which then merge
 353 and grow to become larger in diameter and amplitude, and thus, more energetic. This
 354 process is ~~likely~~ associated with the inverse energy cascade, and ~~suggest suggests~~ that
 355 this mechanism not only drives ~~the~~-EKE seasonality, but also may be responsible ~~of for~~
 356 the seasonal cycle of coherent eddies.

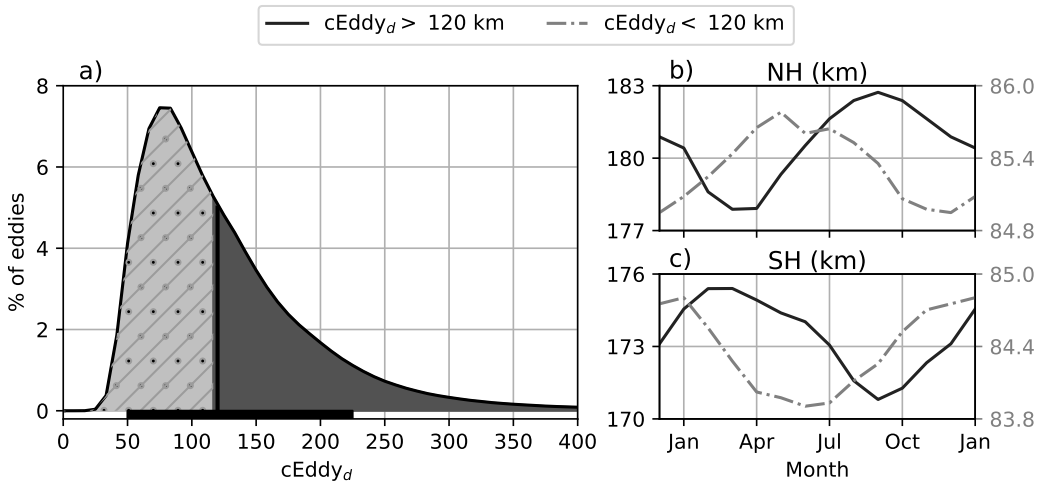
373 Long-term changes can be observed in Figure 6a,b, e, and f where ~~growing shrinking~~
 374 ~~growing/shrinking~~ concentric circles over time denote an ~~increase decrease increase/decrease~~
 375 trend of the field. This trend is particularly evident in the Southern Hemisphere, where
 376 the number of eddies has decreased, ~~while~~ the eddy amplitude has increased. This re-
 377 sult is consistent with the observed trends in EKE and mesoscale EKE in the Southern
 378 Ocean ([Hogg et al., 2015; Martínez-Moreno et al., 2019](#))[\(Hogg et al., 2015; Martínez-Moreno et al., 2019\)](#)
 379 . The coherent eddy amplitude from positive coherent eddies and negative coherent ed-
 380 dies show similar seasonal cycles to the absolute eddy amplitude. The Northern Hemi-
 381 sphere decrease in absolute eddy amplitude is driven by a decrease of the amplitude of
 382 negative coherent eddies in the Northern Hemisphere. Meanwhile in the Southern Ocean,
 383 the increase in absolute eddy amplitude is corroborated by ~~an a~~ strengthening of both
 384 coherent eddy polarities since the early 90s.

385 5 Trends

386 The results presented in Figures 4 and 6 suggest a long-term readjustment of the
 387 coherent eddy field. The long-term trends of the number of coherent eddies, absolute co-
 388 herent eddy amplitude, and coherent eddy amplitude polarities are [further](#) explored in
 389 Figure 8 . ~~Chelton's and M-M contrasting the MM19 and CS13 methods. MM19 and~~
 390 [CS13](#) datasets show consistent spatial patterns in the trends and significance of the num-
 391 ber of coherent eddies and the absolute coherent eddy amplitude. Several regions in the
 392 ocean, such as the Southern Ocean, North Atlantic and North Pacific, show a decrease
 393 in the number of eddies. Those same regions also have a clear increase in the absolute
 394 coherent eddy amplitude. These trends are similar to those observed in mesoscale eddy
 395 kinetic energy (Martínez-Moreno et al., 2021) and provide additional evidence of a read-
 396 justment of the mesoscale eddy field over the last 3 decades.



357 **Figure 6.** Seasonality of the count of number of eddies ($c\text{Eddy}_n$) and area-weighted the
 358 area-weighted polarity independent coherent eddy amplitude ($\langle |c\text{Eddy}_{amp}| \rangle$); Panels a and b
 359 show the time-series of the Northern Hemisphere, while panels e and f correspond to the South-
 360 ern Hemisphere. Panels c and d show the seasonal cycle of the $c\text{Eddy}_n$ and $\langle |c\text{Eddy}|_{amp} \rangle_{NH}$
 361 in the Northern Hemisphere, and panels g and h show the Southern Hemisphere ($c\text{Eddy}_n$ and
 362 $\langle |c\text{Eddy}|_{amp} \rangle_{SH}$). Dashed lines correspond to the seasonal cycle of the fields and dotted lines
 363 show the seasonal cycle of the wind magnitude smoothed over 120 days (moving average). The
 364 black and magenta markers (circle and bar) show indicate the maximum of the seasonal cycle for
 365 the eddy property, and the wind magnitude, respectively. In the cyclic plots, line colors shows
 366 show the year from 1993-2019.

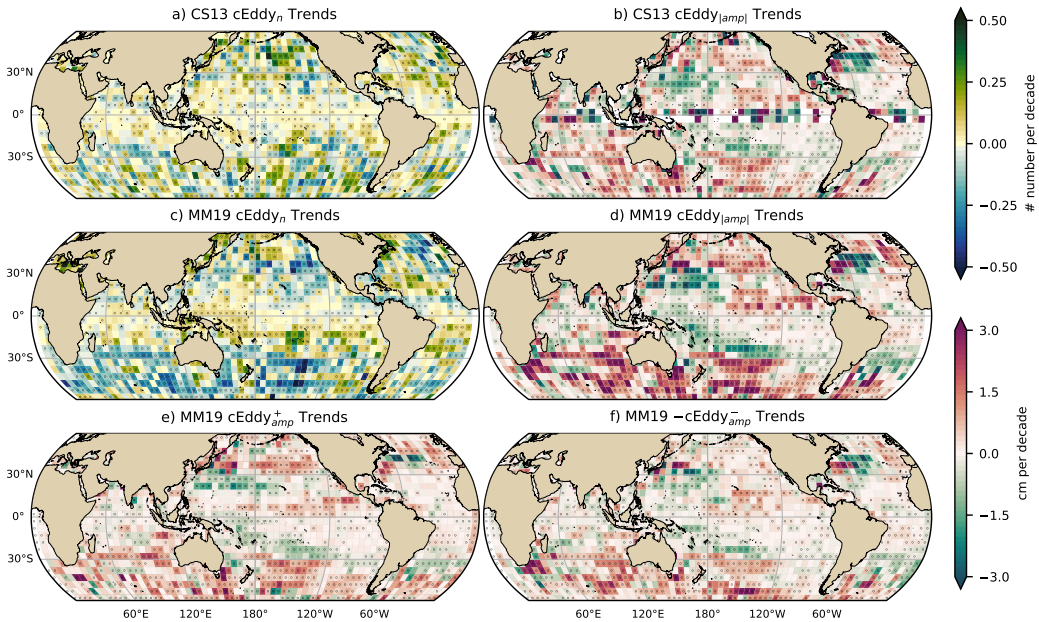


367 **Figure 7.** Distribution of the identified eddy diameter ($cEddy_d$; km) and hemispherical
 368 seasonality of the coherent eddy diameter. a) Distribution in percentage of identified eddy ampli-
 369 tude, solid bar ~~bellow~~^{below} distribution represents 90% of the identified eddies. Seasonal cycle
 370 of the eddy diameter for the b) Northern Hemisphere and c) Southern Hemisphere. Dark solid
 371 line and area corresponds to coherent eddies with diameters larger than 120 km, while light gray
 372 dash-dotted line and area shows coherent eddies with diameters smaller than 120 km.

397 *@Matt: What do you think? Is it important to highlight the trends we observe are different to sea level rise?*

398

399 The observed trends of $cEddy_{amp}$ in several oceanic regions have the same scale
 400 as sea level rise ($\sim 3\text{cm per decade}$)~~by~~. By analyzing the positive and negative coher-
 401 ent eddy amplitude~~we can discard~~, ~~we filter out~~ the observed trends ~~correspond to an~~
 402 ~~that come from a net~~ increase in sea level. In fact, each coherent eddy polarity has in-
 403 tensified in the Southern Ocean and North East Pacific and Atlantic. In other words,
 404 the amplitude of each polarity has increased over time, ~~and~~ thus this strengthening is
 405 an intrinsic response of the coherent eddy field. Note that the negative coherent eddy
 406 amplitude dominates the global $|cEddy_{amp}|$ trends (Figure 8e, f). However, different trend
 407 ~~pattern~~^{patterns} can be observed in both positive and negative coherent eddy amplitudes
 408 in the ~~north Atlantic and north~~^{North} Atlantic and North Pacific, where the negative
 409 coherent eddy amplitude in the Western Boundary Currents appears to decrease.



410 **Figure 8.** Trends of coherent eddy statistics. a) and b) Trends of the number of identified
 411 coherent eddies from satellite observations identified using [the TrackEddy scheme of MM19](#), and
 412 those reported in [CheltonCS13](#)'s dataset. c) and d) Trends of the absolute value of identified co-
 413 herent [eddies](#) [amplitude](#) ($cEddy_{amp}$) from satellite observations identified using TrackEddy
 414 ([after MM19](#)), and those reported [in Chelton's dataset by CS13](#). e) and f) Trends of [the](#) eddy
 415 amplitude polarity using TrackEddy ($cEddy_{amp}^+$ and $cEddy_{amp}^-$). Gray stippling shows regions
 416 that are statistically significant above the 95% confidence level.

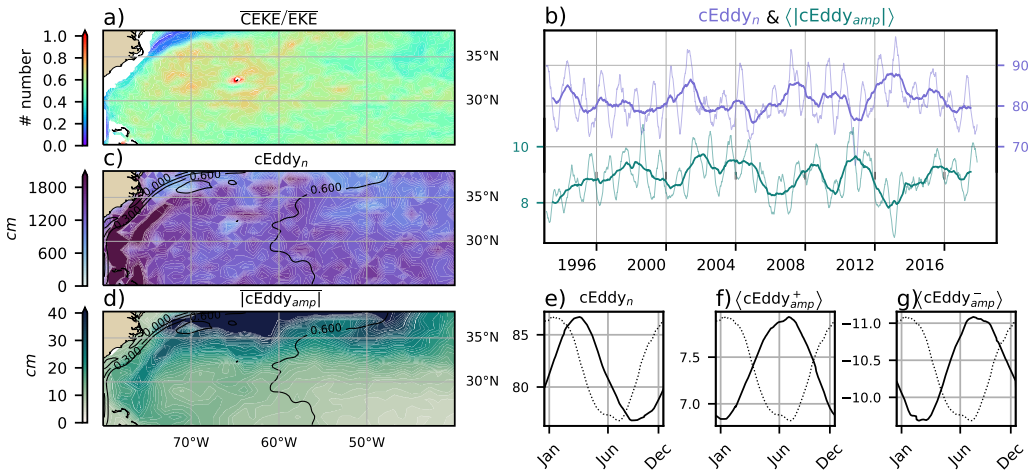
417 6 Regional Climatology

418 For regions with relatively large proportions of CEKE located at ~~boundary extensions~~
 419 ~~and eastern~~ WBCe and eastern boundary currents, we investigate the seasonal and long-
 420 term variability of the coherent eddy properties.

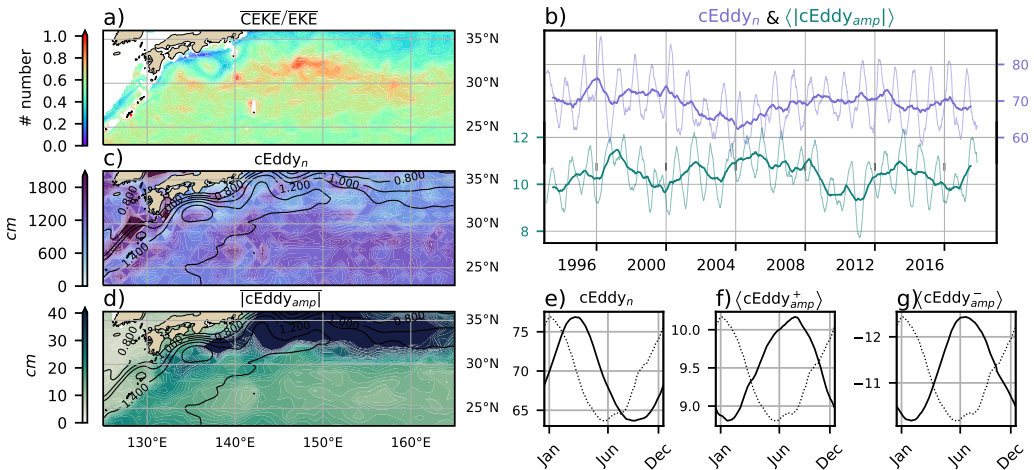
421 The most energetic ~~western boundary extensions include~~; WBCe include the Gulf
 422 Stream, the Kuroshio Current, and the Agulhas Current (Figures 9, 10, and 11). Coher-
 423 ent eddy generation in boundary current extensions occurs through baroclinic and barotropic
 424 instabilities of the mean current, thus all these regions share similar generation dynam-
 425 ics. In all these regions without exception; (i) CEKE contains ~~up to 80~~50-80% of the EKE
 426 in regions ~~equatorwards~~ equatorward from the mean ~~western boundary extension location~~ WBCe,
 427 (ii) the number of eddies is consistently ~~minimal numbers of eddies~~ small over the mean
 428 ~~western boundary extension location~~ WBCe, and (iii) the eddy amplitude is larger ~~polewards~~
 429 ~~of the mean western boundary extension location~~ over the mean WBCe.

430 In the Gulf Stream, the energy ratio between CEKE and EKE is \sim 56% (Figure 9).
 431 The highest energy ~~content ratio~~ occurs in regions with numerous eddies, ~~and~~ collocated
 432 with regions where the largest $|cEddy_{amp}|$ gradients ~~oeurs occur~~. The time series of $cEddy_n$
 433 and $\langle |cEddy_{amp}| \rangle$ are anti-correlated (-0.52), and they display ~~inter-annual~~ interannual
 434 and seasonal variability. Although Chaudhuri et al. (2009) observed ~~that~~ a positive phase
 435 of ~~the~~ North Atlantic Oscillation (NAO) ~~exhibit exhibits~~ higher EKE, due to an increase
 436 in baroclinic ~~instabilities~~ instability, thus suggesting more coherent eddies, we do not find
 437 a correlation between the $cEddy_n$ or the $\langle |cEddy_{amp}| \rangle$ in the Gulf Stream and the NAO
 438 index. Similar to the signal observed in the ~~hemispherical~~ hemispheric analysis, the eddy
 439 count seasonal cycle follows the wind maximum ~~after lagging by~~ \sim 3 months, while the
 440 amplitude of the coherent eddies lags by \sim 6 months.

449 The variability of the $cEddy_n$ and $\langle |cEddy_{amp}| \rangle$ in the Kuroshio Current are weakly
 450 anti-correlated (-0.41; Figure 10). However, on average 56% of the energy in the region
 451 corresponds to CEKE. As observed in the Gulf Stream, there is an important seasonal
 452 cycle in the boundary ~~extension~~ extension, where the eddy count seasonal cycle occurs
 453 ~~on March after ~3 months of in March, lagging~~ the wind maximum ~~by ~3 months~~ (Jan-
 454 uary). Meanwhile, the amplitude of the coherent eddies lags ~~the wind maximum~~ by \sim
 455 6 months (June) ~~after the maximum wind~~.



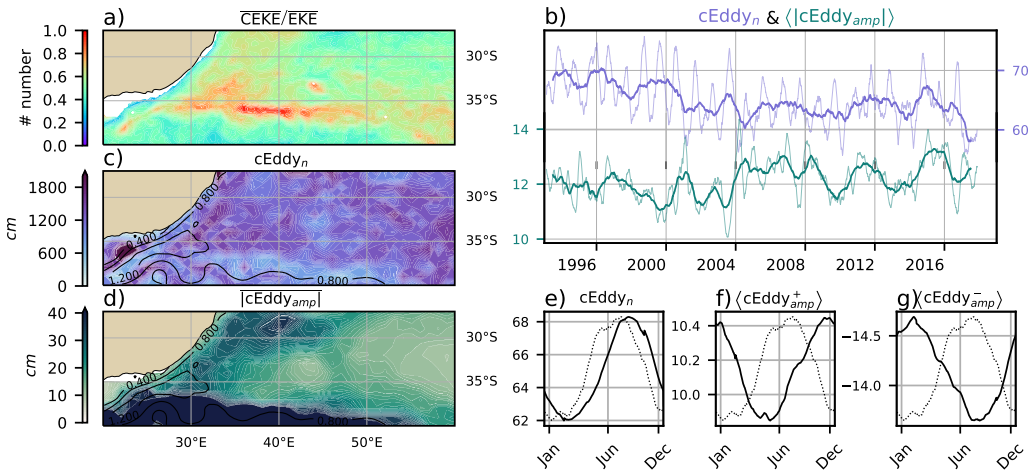
441 **Figure 9.** Climatology of the eddy field and coherent eddy field ~~at-in~~ in the Gulf Stream. a)
442 Ratio of mean coherent eddy kinetic energy ($\overline{\text{CEKE}}$) versus mean eddy kinetic energy ($\overline{\text{EKE}}$);
443 b) Thick lines show the running average over 2 years and thin lines show the running average
444 over 90 days of the coherent eddy number sum and the average coherent eddy amplitude; c)
445 Map of the number of eddies; d) Map of the average coherent eddy amplitude; e) Seasonal cycle
446 of the number of eddies ($\langle \text{cEddy}_n \rangle$); f) Seasonal cycle of the positive coherent eddy amplitude $\langle \langle \text{cEddy}_{amp}^+ \rangle \rangle$, and
447 g) Seasonal cycle of the negative coherent eddy amplitude $\langle \langle \text{cEddy}_{amp}^- \rangle \rangle$.
448 Contours in maps correspond to mean sea surface height (m).



456 **Figure 10.** Climatology As in Figure 9, climatology of the eddy field and coherent eddy field
 457 at in the Kuroshio extension. a) Ratio of mean coherent eddy kinetic energy (\overline{CEKE}) versus
 458 mean eddy kinetic energy (\overline{EKE}); b) Time-series of the coherent eddy number and the average
 459 coherent eddy amplitude; c) Map of the number of eddies; d) Map of the average coherent eddy
 460 amplitude; Seasonal cycle of the e) number of eddies; f) positive coherent eddy amplitude, and
 461 g) negative coherent eddy amplitude. Different lines represent the same as in Figure 9.

462 In the Southern Hemisphere, the strongest boundary current, the Agulhas Cur-
 463 rent, shows similar behavior to its counterparts in the Northern Hemisphere (Figure 11).
 464 On average, coherent eddies in the Agulhas current Current contain $\sim 56\%$ of the energy,
 465 meanwhile the $cEddy_n$ seasonal peak occurs in August, while the $\langle |cEddy_{amp}| \rangle$ peak oc-
 466 curs in January–February. The seasonal lag between the winds, eddy count, and eddy
 467 amplitude in each of the western boundary current extensions WBCe is interpreted as
 468 being analogous to the explanation observed in Figure 6 of the lagged response of co-
 469 herent eddy properties (Figure 6) due to eddy-eddy interactions, consistent with the in-
 470 verse cascade of energy.

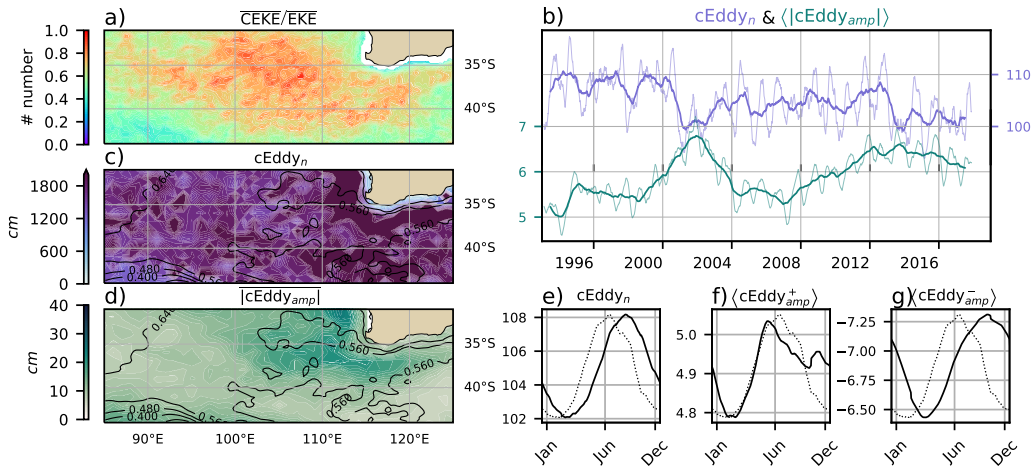
477 Coherent eddies dominate the EKE field in other regions such as the Leeuwin Cur-
 478 rent (Figure 12), where ~~the~~ 65% of the energy is contained by coherent eddies. Although
 479 ~~the~~ The Leeuwin region is not characterized by having a large EKE, however, a consid-
 480 erable abundance of eddies and large eddy amplitudes are observable observed in the re-
 481 gion. The series time-series reveal a significant increase in the $\langle |cEddy_{amp}| \rangle$, while the
 482 $cEddy_n$ has decreased over the last 3 decades ~~(@Andy, you suggested a reference here, I couldn't find it....)~~



471 **Figure 11.** As in Figure 9, Climatology of the eddy field and coherent eddy field at in the Ag-
 472 ulhas Current. a) Ratio of mean coherent eddy kinetic energy (\overline{CEKE}) versus mean eddy kinetic
 473 energy (\overline{EKE}); b) Time-series of the coherent eddy number and the average coherent eddy ampli-
 474 tude; c) Map of the number of eddies; d) Map of the average coherent eddy amplitude; Seasonal
 475 cycle of the e) number of eddies; f) positive coherent eddy amplitude, and g) negative coherent
 476 eddy amplitude. Different lines represent the same as in Figure 9.

483 The seasonal cycle shows that the $cEddy_n$ peak occurs on in August, 3 months after the
 484 maximum winds (June). Meanwhile, the $\langle cEddy_{amp}^+ \rangle$ responds in synchrony to the winds,
 485 and the $\langle cEddy_{amp}^- \rangle$ is in phase with the seasonal cycle of the eddy number ($cEddy_n^-$).
 486 Hence, this region contrast the behavior of WBCe, and showcases the spatial variability
 487 of the seasonal cycle of coherent eddies.

488 Another region with important contributions of to the coherent eddy field is the
 489 East Tropical Pacific (Tehuantepec region; Figure 13), where coherent eddies contain ~58%
 490 of the energy. In fact, coherent eddy generation in this region is modulated by winds and
 491 coastally trapped waves which produce a strong horizontal and vertical shear
 492 (baroclinic and barotropic instabilities; Zamudio et al., 2006). Furthermore, the equa-
 493 torial generated waves propagating along the coast have an important interannual vari-
 494 ability observable in the $\langle |cEddy_{amp}| \rangle$ time-series, where El Niño events are notable dur-
 495 ing 1997 and 2015 (Figure 13b). The seasonal cycle of $cEddy_n$, $\langle cEddy_{amp}^+ \rangle$, and $\langle cEddy_{amp}^- \rangle$
 496 support the idea of a coherent eddies responding eddy response to two different coher-
 497 ent eddy generation mechanisms; the number of eddies seasonal cycle lags for lags by ~3
 498

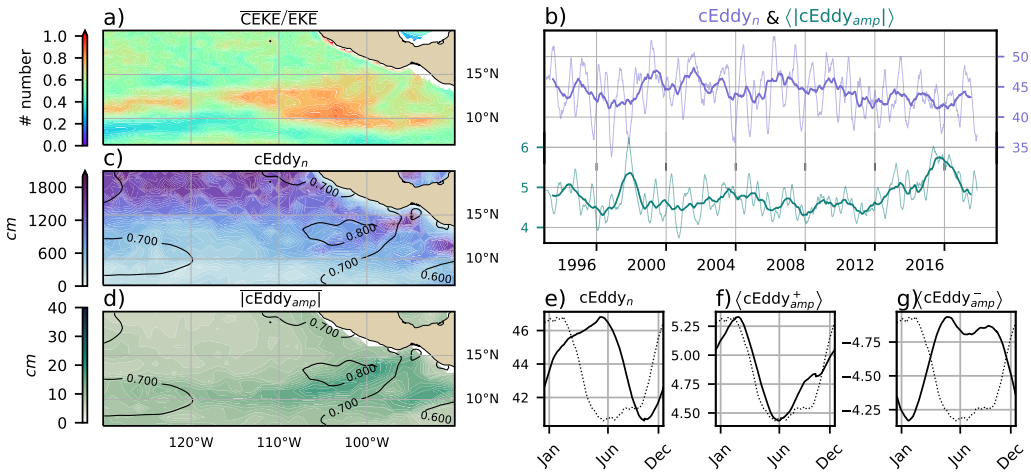


488 **Figure 12.** *Climatology As in Figure 9, climatology* of the eddy field and coherent eddy field
 489 *at in* the Leeuwin Current. a) Ratio of mean coherent eddy kinetic energy ($\overline{\text{CEKE}}$) versus mean
 490 eddy kinetic energy ($\overline{\text{EKE}}$); b) Time-series of the coherent eddy number and the average coherent
 491 eddy amplitude; c) Map of the number of eddies; d) Map of the average coherent eddy amplitude;
 492 Seasonal cycle of the e) number of eddies; f) positive coherent eddy amplitude, and g) negative
 493 coherent eddy amplitude. *Different lines represent the same as in Figure 9.*

504 months from the winds, while the $\langle \text{cEddy}_{amp}^+ \rangle$ is *on-in* phase with the winds and the *maximum*
 505 *of trapped-waves time of maximum trapped wave activity* (winter; Zamudio et al., 2006),
 506 *and while* the $\langle \text{cEddy}_{amp}^- \rangle$ could be a consequence of eddy-eddy interactions.

513 7 Discussion and Conclusions

514 We *have* investigated the contribution of coherent eddies *in the to the total* kinetic
 515 energy field using *available* satellite observations. We *erroborate*-*found* that around half
 516 of the EKE is explained by coherent eddies. This half is concentrated in eddy-rich re-
 517 gions where *an-a recent multi-decadal* intensification of the eddy field has been observed
 518 (Martínez-Moreno et al., 2021). The energy contained by eddies is larger than the pre-
 519 vious estimate of 40% by Chelton et al. (2011). Although there are *difference-differences*
 520 in the identification criteria of both eddy identification methods, the main cause of the
 521 difference is *believed likely* to be the lifespan and amplitude filters. These filters are widely
 522 used to track individual eddies *on-in* space and time, however, interactions between ed-
 523 dies in energetic regions *my-may* obscure the abundance and influence of short-lived co-



507 **Figure 13.** Climatology As in Figure 9, climatology of the eddy field and coherent eddy field
 508 at in the East Tropical Pacific. a) Ratio of mean coherent eddy kinetic energy (\overline{CEKE}) versus
 509 mean eddy kinetic energy (\overline{EKE}); b) Time-series of the coherent eddy number and the average
 510 coherent eddy amplitude; c) Map of the number of eddies; d) Map of the average coherent eddy
 511 amplitude; Seasonal cycle of the e) number of eddies; f) positive coherent eddy amplitude, and
 512 g) negative coherent eddy amplitude. Different lines represent the same as in Figure 9.

524 herent eddies. Filters are not used in this study, and indeed a lack of filters could facilitates
 525 an under or facilitate an over-estimation of the the energy contained by coherent eddies,
 526 when miss-identifying or miss-fitting mis-identifying or mis-fitting a coherent eddy. Thus,
 527 In hindsight, current generation of climate models have just started to resolve mesoscale
 528 dynamics, thus, the presented estimate represents an upper limit of of energy in coherent
 529 eddies from satellite observations could be used as a benchmark and quantify the energy
 530 contained by coherent eddiesmesoscale and more specifically coherent eddies in future
 531 climate models.

532 In addition, it should It should also be noted that regions with first baroclinic Rossby
 533 radius of deformation smaller than 10km cannot be resolved by satellite observations.
 534 Thus, the energy contained by coherent eddies around latitudes of 60° and those near
 535 the shore are missed from this estimate, and remains unknown their role in the seasonal
 536 cycle and local dynamics remains unknown . New satellite altimeter missions (e.g. Surface
 537 Water and Ocean Topography; SWOT) may allow to estimate estimates of the energy

538 contained by mesoscale coherent eddies outside the tropical region and the continental
 539 slope.

540 ~~Hemispherical Hemisphere-wide~~ variability indicates a strong seasonal cycle of the
 541 EKE, CEKE, and eddy properties. The seasonal cycle of the CEKE in each hemisphere
 542 occurs as a consequence of numerous small coherent eddies interacting with each other
 543 (eddy-eddy interactions) and resulting in stronger, larger and more energetic ~~(but fewer)~~
 544 coherent eddies during summer, after a few months of the yearly coherent eddy number
 545 maxima. This ~~results~~ result reveals eddy-eddy interactions and thus the transfer of en-
 546 ergy from smaller coherent eddies to larger coherent eddies could explain the observed
 547 seasonal cycle of CEKE and coherent eddies properties.

548 Coherent eddy properties ~~showcase reveal~~ a non-uniform long-term readjustment
 549 of the mesoscale eddy field. Overall, the eddy number has decreased globally at a sig-
 550 nificant rate of ~ 35 eddies per decade from ~ 4000 eddies identified globally on average
 551 each day. ~~However~~ Despite the small changes in the eddy numbers, large proportions of
 552 the ocean show ~~an~~ a major strengthening of the mesoscale coherent eddy ~~field at a rate~~
 553 amplitude at rates greater than ~ 1 cm per decade. This strengthening of the coherent
 554 eddy amplitude is attributed to an intensification of each coherent eddy polarity, rather
 555 than a readjustment of the coherent eddy field to sea level rise. In other words, the co-
 556 herent eddy amplitude intensification is occurring in both coherent eddy polarities and
 557 ~~explain~~ explains a proportion of the previously observed readjustments in the eddy field
 558 to long-term changes in the ocean forcing (Hu et al., 2020; Wunsch, 2020; Martínez-Moreno
 559 et al., 2021). This long-term readjustment ~~showcases reveals~~ an intensification of the co-
 560 herent eddy field, possibly due to long-term readjustments in the ocean baroclinic and
 561 barotropic instabilities, as well as the strength of the winds.

562 The reconstruction of the coherent eddies and their statistics ~~have has~~ revealed re-
 563 gions with important coherent eddy contributions and a distinct seasonal evolution of
 564 the coherent eddies. ~~Remarkably, western boundary extensions~~ Western boundary current
 565 extensions (WBCe) generate eddies through the instability of the main currents and the
 566 seasonal cycle of coherent eddies, CEKE, and thus EKE could be associated with an in-
 567 verse energy cascade observable through lagged seasonal cycles in the coherent eddy statis-
 568 tics. In addition ~~to this~~, the amplitude of the seasonal cycle in ~~the boundary extensions~~
 569 WBCe is two times larger than any other region, thus the seasonality of the coherent ed-

570 dies in boundary extensions dominate the hemispherical WBCe dominates the hemispheric
 571 seasonal cycle. Furthermore, the seasonal lag of the inverse energy cascade is coupled
 572 with the presence of fronts (Qiu et al., 2014), such is the case of western boundary extensions for
 573 WBCe, and our results are consistent with the notion of baroclinic instability generating
 574 eddies and through via eddy-eddy interactions and a lagged inverse energy cascade.

575 The use of satellite observations in this study limit limits our ability to quantify
 576 the importance of the inverse energy cascade seasonality in the control of the coherent
 577 eddy seasonal cycle. As mentioned above, there is robust evidence of an increase in eddy-
 578 eddy interactions, however we can not cannot discard important contributions from other
 579 processes such as the seasonal cycle of forcing, stratification, and instabilities, which are
 580 crucial in the generation of coherent eddies. Although this study can provide a descriptive
 581 response of the coherent eddy field, further studies work is needed to asses the
 582 role of eddy-eddy interactions in our changing climate, ocean dynamics, and biogeochemical
 583 process. Furthermore, the SWOT mission could allow us to advance our understanding
 584 of eddy-eddy interactions and the seasonal cycle of scales smaller than mesoscale, which
 585 may provide further evidence of the inverse energy cascade driving the coherent eddy
 586 seasonality.

587 Acknowledgments

588 The Chelton & Schlax (2013) dataset was produced by SSALTO/DUACS and distributed
 589 by AVISO+ (<https://www.aviso.altimetry.fr/>) with support from CNES, developed
 590 and validated in collaboration with E.Mason at IMEDEA. Global coherent eddy recon-
 591 struction, coherent and non-coherent non-coherent eddy kinetic energy datasets, in ad-
 592 dition to gridded coherent eddy tracking datasets are publicly available at (<https://doi.org/10.5281/zenodo.4646429>). All analyses and figures in this manuscript are re-
 593 producible via Jupyter notebooks and instructions can be found in the Github repos-
 594 itory CEKE_climatology (https://github.com/josuemtzmo/CEKE_climatology). Trends
 595 used the Python Package xarrayMannKendall (<https://doi.org/10.5281/zenodo.4458776>).
 596 J.M.-M. was supported by the Consejo Nacional de Ciencia y Tecnología (CONACYT),
 597 Mexico funding. M.H.E. is supported by the Centre for Southern Hemisphere Oceans
 598 Research (CSHOR), a joint research centre between Qingdao National Laboratory for
 599 Marine Science and Technology (QNLMT), Commonwealth Scientific and Industrial Research
 600 Organisation (CSIRO), University of New South Wales (UNSW), and the University of

602 Tasmania (UTAS). Analyses were undertaken on the National Computational Infrastructure
 603 in Canberra, Australia, which is supported by the Australian Commonwealth Government.
 604

605 **References**

- 606 Arbic, B. K., Polzin, K. L., Scott, R. B., Richman, J. G., & Shriver, J. F. (2013).
 607 On Eddy Viscosity, Energy Cascades, and the Horizontal Resolution of Gridded
 608 Satellite Altimeter Products*. *Journal of Physical Oceanography*, 43(2), 283–300.
 609 doi: 10.1175/jpo-d-11-0240.1
- 610 Ashkezari, M. D., Hill, C. N., Follett, C. N., Forget, G., & Follows, M. J. (2016).
 611 Oceanic eddy detection and lifetime forecast using machine learning methods.
 612 *Geophysical Research Letters*, 43(23). doi: 10.1002/2016gl071269
- 613 Beron-Vera, F. J., Wang, Y., Olascoaga, M. J., Goni, G. J., & Haller, G. (2013). Ob-
 614 jective Detection of Oceanic Eddies and the Agulhas Leakage. *Journal of Physical
 615 Oceanography*, 43(7), 1426–1438. doi: 10.1175/JPO-D-12-0171.1
- 616 Bouali, M., Sato, O. T., & Polito, P. S. (2017). Temporal trends in sea surface tem-
 617 perature gradients in the South Atlantic Ocean. *Remote Sensing of Environment*,
 618 194, 100–114. doi: 10.1016/j.rse.2017.03.008
- 619 Callies, J., Flierl, G., Ferrari, R., & Fox-Kemper, B. (2015). The role of mixed-layer
 620 instabilities in submesoscale turbulence. *Journal of Fluid Mechanics*, 788, 5–41.
 621 doi: 10.1017/jfm.2015.700
- 622 Cane, M. A., Clement, A. C., Kaplan, A., Kushnir, Y., Pozdnyakov, D., Seager, R.,
 623 ... Murtugudde, R. (1997). Twentieth-Century Sea Surface Temperature Trends.
 624 *Science*, 275(5302), 957–960. doi: 10.1126/science.275.5302.957
- 625 Chaudhuri, A. H., Gangopadhyay, A., & Bisagni, J. J. (2009). Interannual variabil-
 626 ity of Gulf Stream warm-core rings in response to the North Atlantic Oscillation.
 627 *Continental Shelf Research*, 29(7), 856–869. doi: 10.1016/j.csr.2009.01.008
- 628 Chelton, D. B., A, d. R., Schlax, M. G., Naggar, K., & Siwertz, N. (1998). Geo-
 629 graphical variability of the first baroclinic Rossby radius of deformation. *Journal
 630 of Physical Oceanography*, 28(3), 433–460. doi: 10.1175/1520-0485(1998)028<433:
 631 GVOTFB>2.0.CO;2
- 632 Chelton, D. B., Gaube, P., Schlax, M. G., Early, J. J., & Samelson, R. M. (2011).
 633 The influence of nonlinear mesoscale eddies on near-surface oceanic chlorophyll.

- 634 *Science*, 334(6054), 328-32. doi: 10.1126/science.1208897

635 Chelton, D. B., & Schlax, M. G. (2013). *Mesoscale eddies in altimeter observations*

636 *of ssh*.

637 Chelton, D. B., Schlax, M. G., Samelson, R. M., & de Szoeke, R. A. (2007). Global

638 observations of large oceanic eddies. *Geophysical Research Letters*, 34(15),

639 L15606. doi: 10.1029/2007GL030812

640 CMEMS. (2017). The Ssalto/Duacs altimeter products were produced and dis-

641 tributed by the Copernicus Marine and Environment Monitoring Service. *Aviso*

642 *Dataset*. Retrieved from <https://www.aviso.altimetry.fr/>

643 Cui, W., Wang, W., Zhang, J., & Yang, J. (2020). Identification and census statis-

644 tics of multicore eddies based on sea surface height data in global oceans. *Acta*

645 *Oceanologica Sinica*, 39(1), 41–51. doi: 10.1007/s13131-019-1519-y

646 Faghmous, J. H., Frenger, I., Yao, Y., Warmka, R., Lindell, A., & Kumar, V. (2015,

647 6). A daily global mesoscale ocean eddy dataset from satellite altimetry. *Scientific*

648 *Data*, 2, 150028 EP -. doi: 10.1038/sdata.2015.28

649 Ferrari, R., & Wunsch, C. (2009). Ocean Circulation Kinetic Energy: Reservoirs,

650 Sources, and Sinks. *Annual Review of Fluid Mechanics*, 41(1), 253–282. doi: 10

651 .1146/annurev.fluid.40.111406.102139

652 Frenger, I., Gruber, N., Knutti, R., & Münnich, M. (2013). Imprint of Southern

653 Ocean eddies on winds, clouds and rainfall. *Nature Geoscience*, 6(8), 608 EP -. doi: 10.1038/ngeo1863

654 Frenger, I., Münnich, M., Gruber, N., & Knutti, R. (2015). Southern Ocean eddy

655 phenomenology. *Journal of Geophysical Research: Oceans*, 120(11), 7413-7449.

656 doi: 10.1002/2015JC011047

658 Fu, L., Chelton, D., Le Traon, P., & Oceanography, M. R. (2010). Eddy dynamics

659 from satellite altimetry. *Oceanography*, 23(4), 14-25. doi: 10.2307/24860859

660 Gill, A., Green, J., & Simmons, A. (1974). Energy partition in the large-scale ocean

661 circulation and the production of mid-ocean eddies. *Deep Sea Res Oceanogr Abstr*,

662 21(7), 499-528. doi: 10.1016/0011-7471(74)90010-2

663 Hogg, A. M., & Blundell, J. R. (2006). Interdecadal variability of the southern

664 ocean. *Journal of Physical Oceanography*, 36(8), 1626-1645. doi: 10.1175/JPO2934.1

666 Hogg, A. M., Meredith, M. P., Chambers, D. P., Abrahamsen, E. P., Hughes,

- 667 C. W., & Morrison, A. K. (2015). Recent trends in the Southern Ocean
668 eddy field. *Journal of Geophysical Research: Oceans*, 120(1), 257-267. doi:
669 10.1002/2014JC010470
- 670 Hu, S., Sprintall, J., Guan, C., McPhaden, M. J., Wang, F., Hu, D., & Cai,
671 W. (2020, 2). Deep-reaching acceleration of global mean ocean circula-
672 tion over the past two decades. *Science Advances*, 6(6), eaax7727. doi:
673 10.1126/sciadv.aax7727
- 674 Japan Meteorological Agency, Japan. (2013). *Jra-55: Japanese 55-year reanalysis,*
675 *daily 3-hourly and 6-hourly data.* Boulder CO: Research Data Archive at the Na-
676 tional Center for Atmospheric Research, Computational and Information Systems
677 Laboratory. Retrieved from <https://doi.org/10.5065/D6HH6H41>
- 678 Kang, D., & Curchitser, E. N. (2013). Gulf stream eddy characteristics in a high-
679 resolution ocean model. *Journal of Geophysical Research: Oceans*, 118(9), 4474-
680 4487. Retrieved from <https://agupubs.onlinelibrary.wiley.com/doi/abs/10.1002/jgrc.20318> doi: <https://doi.org/10.1002/jgrc.20318>
- 682 Kang, D., & Curchitser, E. N. (2017). On the Evaluation of Seasonal Variability of
683 the Ocean Kinetic Energy. *Geophysical Research Letters*, 47, 1675-1583. doi: 10
684 .1175/JPO-D-17-0063.1
- 685 Li, G., Cheng, L., Zhu, J., Trenberth, K. E., Mann, M. E., & Abraham, J. P. (2020).
686 Increasing ocean stratification over the past half-century. *Nature Climate Change*,
687 1–8. doi: 10.1038/s41558-020-00918-2
- 688 Martínez-Moreno, J., Hogg, A. M., England, M., Constantinou, N. C., Kiss, A. E.,
689 & Morrison, A. K. (2021). Global changes in oceanic mesoscale currents over the
690 satellite altimetry record. *Journal of Advances in Modeling Earth Systems*, 0(ja).
691 doi: 10.1029/2019MS001769
- 692 Martínez-Moreno, J., Hogg, A. M., Kiss, A. E., Constantinou, N. C., & Morrison,
693 A. K. (2019). Kinetic energy of eddy-like features from sea surface altime-
694 try. *Journal of Advances in Modeling Earth Systems*, 11(10), 3090-3105. doi:
695 10.1029/2019MS001769
- 696 Patel, R. S., Llort, J., Strutton, P. G., Phillips, H. E., Moreau, S., Pardo, P. C.,
697 & Lenton, A. (2020). The Biogeochemical Structure of Southern Ocean
698 Mesoscale Eddies. *Journal of Geophysical Research: Oceans*, 125(8). doi:
699 10.1029/2020jc016115

- 700 Pilo, G. S., Mata, M. M., & Azevedo, J. L. L. (2015). Eddy surface properties and
701 propagation at Southern Hemisphere western boundary current systems. *Ocean
702 Science*, 11(4), 629–641. doi: 10.5194/os-11-629-2015
- 703 Qiu, B. (1999). Seasonal Eddy Field Modulation of the North Pacific Subtropical
704 Countercurrent: TOPEX/Poseidon Observations and Theory. *Journal of Physical
705 Oceanography*, 29(10), 2471–2486. doi: 10.1175/1520-0485(1999)029<2471:sefmot>2
706 .0.co;2
- 707 Qiu, B., & Chen, S. (2004). Seasonal Modulations in the Eddy Field of the South
708 Pacific Ocean. *Journal of Physical Oceanography*, 34(7), 1515–1527. doi: 10.1175/
709 1520-0485(2004)034<1515:smitef>2.0.co;2
- 710 Qiu, B., Chen, S., Klein, P., Sasaki, H., & Sasai, Y. (2014). Seasonal Mesoscale
711 and Submesoscale Eddy Variability along the North Pacific Subtropical Coun-
712 tercurrent. *Journal of Physical Oceanography*, 44(12), 3079–3098. doi:
713 10.1175/JPO-D-14-0071.1
- 714 Ruela, R., Sousa, M. C., deCastro, M., & Dias, J. M. (2020). Global and regional
715 evolution of sea surface temperature under climate change. *Global and Planetary
716 Change*, 190, 103190. doi: 10.1016/j.gloplacha.2020.103190
- 717 Sasaki, H., Klein, P., Qiu, B., & Sasai, Y. (2014). Impact of oceanic-scale inter-
718 actions on the seasonal modulation of ocean dynamics by the atmosphere. *Nature
719 Communications*, 5(1), 5636. doi: 10.1038/ncomms6636
- 720 Schubert, R., Schwarzkopf, F. U., Baschek, B., & Biastoch, A. (2019). Submesoscale
721 Impacts on Mesoscale Agulhas Dynamics. *Journal of Advances in Modeling Earth
722 Systems*, 11(8), 2745–2767. doi: 10.1029/2019ms001724
- 723 Siegel, D., Peterson, P., DJ, M., Maritorena, S., & Nelson, N. (2011). Bio-optical
724 footprints created by mesoscale eddies in the Sargasso Sea. *Geophysical Research
725 Letters*, 38(13), n/a-n/a. doi: 10.1029/2011GL047660
- 726 Uchida, T., Abernathey, R., & Smith, S. (2017). Seasonality of eddy kinetic energy
727 in an eddy permitting global climate model. *Ocean Modelling*, 118, 41–58. doi: 10
728 .1016/j.ocemod.2017.08.006
- 729 Wunsch, C. (2020). Is The Ocean Speeding Up? Ocean Surface Energy Trends.
730 *Journal of Physical Oceanography*, 50(11), 1–45. doi: 10.1175/jpo-d-20-0082.1
- 731 Wunsch, C., & Ferrari, R. (2004). Vertical mixing, energy, and the general circula-
732 tion of the oceans. *Annual Review of Fluid Mechanics*, 36(1), 281–314. doi: 10

- 733 .1146/annurev.fluid.36.050802.122121
- 734 Wyrtki, K., Magaard, L., & Hager, J. (1976). Eddy energy in the oceans. *Journal of*
735 *Geophysical Research*, 81(15), 2641-2646. doi: 10.1029/JC081i015p02641
- 736 Yue, S., & Wang, C. (2004). The Mann-Kendall Test Modified by Effective Sample
737 Size to Detect Trend in Serially Correlated Hydrological Series. *Water Resources*
738 *Management*, 18(3), 201–218. doi: 10.1023/b:warm.0000043140.61082.60
- 739 Zamudio, L., Hurlbert, H. E., Metzger, E. J., Morey, S. L., O'Brien, J. J., Tilburg,
740 C., & Zavala-Hidalgo, J. (2006). Interannual variability of Tehuantepec ed-
741 dies. *Journal of Geophysical Research: Oceans (1978–2012)*, 111(C5). doi:
742 10.1029/2005JC003182